

Accurate ab initio potential energy surface, thermochemistry, and dynamics of the F⁻ + CH₃F SN₂ and proton-abstraction reactions

István Szabó, Hajnalka Telekes, and Gábor Czakó

Citation: *The Journal of Chemical Physics* **142**, 244301 (2015); doi: 10.1063/1.4922616

View online: <http://dx.doi.org/10.1063/1.4922616>

View Table of Contents: <http://scitation.aip.org/content/aip/journal/jcp/142/24?ver=pdfcov>

Published by the [AIP Publishing](#)

Articles you may be interested in

[Accurate ab initio potential energy surface, thermochemistry, and dynamics of the Br\(2P, 2P_{3/2}\) + CH₄ → HBr + CH₃ reaction](#)

J. Chem. Phys. **138**, 134301 (2013); 10.1063/1.4797467

[Accurate ab initio potential energy surface, dynamics, and thermochemistry of the F + CH₄ → HF + CH₃ reaction](#)

J. Chem. Phys. **130**, 084301 (2009); 10.1063/1.3068528

[Accurate ab initio potential energy curve of F₂. III. The vibration rotation spectrum](#)

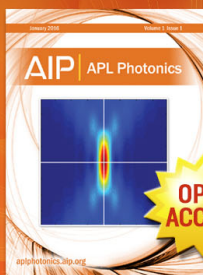
J. Chem. Phys. **127**, 204313 (2007); 10.1063/1.2805392

[The highly anharmonic B H₅ potential energy surface characterized in the ab initio limit](#)

J. Chem. Phys. **122**, 104302 (2005); 10.1063/1.1853377

[Correlated ab initio calculations of spectroscopic parameters of SnO within the framework of the higher-order generalized Douglas–Kroll transformation](#)

J. Chem. Phys. **120**, 8624 (2004); 10.1063/1.1690757



Launching in 2016!
The future of applied photonics research is here

**OPEN
ACCESS**

AIP | APL
Photonics

Accurate *ab initio* potential energy surface, thermochemistry, and dynamics of the $F^- + CH_3F$ S_N2 and proton-abstraction reactions

István Szabó, Hajnalka Telekes, and Gábor Czako^{a)}

Laboratory of Molecular Structure and Dynamics, Institute of Chemistry, Eötvös University, H-1518 Budapest 112, P.O. Box 32, Hungary

(Received 28 April 2015; accepted 4 June 2015; published online 22 June 2015)

We develop a full-dimensional global analytical potential energy surface (PES) for the $F^- + CH_3F$ reaction by fitting about 50 000 energy points obtained by an explicitly correlated composite method based on the second-order Møller–Plesset perturbation-F12 and coupled-cluster singles, doubles, and perturbative triples-F12a methods and the $cc-pVnZ-F12$ [$n = D, T$] basis sets. The PES accurately describes the (a) back-side attack Walden inversion mechanism involving the pre- and post-reaction (b) ion-dipole and (c) hydrogen-bonded complexes, the configuration-retaining (d) front-side attack and (e) double-inversion substitution pathways, as well as (f) the proton-abstraction channel. The benchmark quality relative energies of all the important stationary points are computed using the focal-point analysis (FPA) approach considering electron correlation up to coupled-cluster singles, doubles, triples, and perturbative quadruples method, extrapolation to the complete basis set limit, core-valence correlation, and scalar relativistic effects. The FPA classical(adiabatic) barrier heights of (a), (d), and (e) are $-0.45(-0.61)$, $46.07(45.16)$, and $29.18(26.07)$ kcal mol⁻¹, respectively, the dissociation energies of (b) and (c) are $13.81(13.56)$ and $13.73(13.52)$ kcal mol⁻¹, respectively, and the endothermicity of (f) is $42.54(38.11)$ kcal mol⁻¹. Quasiclassical trajectory computations of cross sections, scattering (θ) and initial attack (α) angle distributions, as well as translational and internal energy distributions are performed for the $F^- + CH_3F(v = 0)$ reaction using the new PES. Apart from low collision energies (E_{coll}), the S_N2 excitation function is nearly constant, the abstraction cross sections rapidly increase with E_{coll} from a threshold of ~ 40 kcal mol⁻¹, and retention trajectories via double inversion are found above $E_{coll} = \sim 30$ kcal mol⁻¹, and at $E_{coll} = \sim 50$ kcal mol⁻¹, the front-side attack cross sections start to increase very rapidly. At low E_{coll} , the indirect mechanism dominates (mainly isotropic backward-forward symmetric θ distribution and translationally cold products) and significant long-range orientation effects (isotropic α distribution) and barrier recrossings are found. At higher E_{coll} , the S_N2 reaction mainly proceeds with direct rebound mechanism (backward scattering and hot product translation). © 2015 AIP Publishing LLC. [<http://dx.doi.org/10.1063/1.4922616>]

I. INTRODUCTION

Bimolecular nucleophilic substitution (S_N2) is one of the best known reaction classes in organic chemistry.^{1,2} The Walden inversion reaction mechanism of the $X^- + CH_3Y$ -type S_N2 reactions is a textbook example of stereo-specific reaction pathways, in which the nucleophile (X^-) attacks the backside of the CH_3Y molecule and replaces the leaving group (Y^-) while the configuration is being inverted around the carbon center. However, recent theoretical and experimental investigations showed that the dynamics is not so simple.^{3–12} Besides the direct rebound mechanism described above, direct stripping (X^- approaches the side of CH_3Y and strips off CH_3), front-side attack (direct replacement of Y^- without inversion), and indirect mechanisms (complex formations, roundabout,⁶ and barrier recrossing) can occur. Moreover, our recent reaction dynamics computations revealed a new double-inversion mechanism for the $F^- + CH_3Cl$ S_N2 reaction.¹² The first step of double inversion is a proton-abstraction induced inversion via a $[XH \cdots CH_2Y]^-$ transition state (TS), which is followed

by a second inversion via the usual $[X \cdots CH_3 \cdots Y]^-$ saddle point, thereby resulting in retention of the initial configuration. Very recently we showed that the $[XH \cdots CH_2Y]^-$ TS (first-order saddle point) exists for all the 16 reactions involving X, Y = F, Cl, Br, and I.¹³ For the $F^- + CH_3Y$ reactions, the double-inversion barrier heights are well below the front-side attack barriers, which are slightly above the $HF + CH_2Y^-$ product asymptotes.¹³ For Y = Cl, our recent reaction dynamics simulations showed that double inversion occurs at low collision energies where the front-side attack pathway is closed.¹²

Atomic-level simulations of S_N2 reactions usually employ the direct dynamics approach,^{3,6,8,14–16} in which the electronic structure computations are performed on-the-fly at each time step of a quasiclassical trajectory (QCT). We use another approach based on analytical potential energy surfaces (PESs) obtained by fitting high-level *ab initio* energy points.^{17,18} We have already developed a full-dimensional global analytical PES for the $F^- + CH_3Cl$ reaction,^{11,12} and in the present study, we apply this approach to the $F^- + CH_3F$ system. The $F^- + CH_3Cl$ S_N2 reaction is highly exothermic with a negative barrier, whereas the $F^- + CH_3F$ system has a symmetric double-well potential. The wells may contain ion-dipole and

^{a)}E-mail: czako@chem.elte.hu

hydrogen-bonded complexes and the central transition state has similar energy to that of the reactants. This PES profile suggests interesting and complicated dynamics, for example, many long-lived trajectories trapped in the entrance and/or exit well and barrier recrossing pathways. Furthermore, at higher collision energies, the double-inversion and front-side attack retention pathways as well as the proton-abstraction channel may open. Experimentally, the abstraction channel could be probed via the detection of the CH_2F^- products, whereas the measurement of the substitution channel is problematic since $\text{F}^- + \text{CH}_3\text{F}$ is an identity $\text{S}_{\text{N}}2$ reaction and fluorine does not have stable isotopes. Theory can study both channels because the simulations can distinguish between the identical atoms.

In Sec. II, we characterize the stationary points of the global PES of the $\text{F}^- + \text{CH}_3\text{F}$ reaction and provide benchmark relative energies employing the composite *ab initio* focal-point analysis (FPA)^{19,20} approach. The FPA method employs a multidimensional extrapolation scheme to approach the complete basis set (CBS) limit of the relativistic all-electron full configuration interaction energy. In Sec. III, we describe the computational details and properties of the full-dimensional global analytical *ab initio* PES of the $\text{F}^- + \text{CH}_3\text{F}$ reaction. With an analytical PES at hand we can efficiently perform QCT computations to study the dynamics of the $\text{F}^- + \text{CH}_3\text{F}$ reaction as described in Sec. IV. The QCT simulations may reveal the different mechanisms of the $\text{F}^- + \text{CH}_3\text{F}$ $\text{S}_{\text{N}}2$ reaction and show the competition between substitution and proton-abstraction at higher collision energies. The paper ends with summary and conclusions in Sec. V.

II. BENCHMARK *AB INITIO* THERMOCHEMISTRY

A. Computational details

The structures and harmonic frequencies of the stationary points are determined at the explicitly correlated AE-CCSD(T)-F12b/cc-pCVTZ-F12 and FC-CCSD(T)-F12b/cc-pVTZ-F12 levels of theory,^{21,22} respectively, where AE denotes all-electron computations, FC means the frozen-core approach (the $1s^2$ electrons of the C and F atoms are not correlated), CCSD(T) is the coupled-cluster (CC) singles, doubles, and perturbative triples method, F12b is a variant of the explicitly correlated methods, and cc-p(C)VTZ-F12 is a correlation-consistent polarized (core)-valence triple zeta basis developed for F12 computations. The FPA^{19,20} relative energies are obtained by single-point computations at the above-defined geometries considering

- extrapolations to the CBS limits of the Hartree–Fock (HF),²³ all-electron second-order Møller–Plesset perturbation theory (AE-MP2),²⁴ AE-CCSD (Ref. 25), and AE-CCSD(T) (Ref. 26) methods using the correlation-consistent aug-cc-pCVnZ [$n = \text{D}(2), \text{T}(3), \text{Q}(4), \text{and } 5$] basis sets,²⁷
- post-CCSD(T) electron correlation effects up to coupled-cluster singles, doubles, triples, and perturbative quadruples method [CCSDT(Q)]²⁸ based on FC-CCSD(T) \rightarrow FC-CCSDT \rightarrow FC-CCSDT(Q) computations with the aug-cc-pVDZ basis, and

- scalar relativistic corrections (Δ_{rel}) as difference between the second-order Douglas–Kroll²⁹ and non-relativistic AE-CCSD(T)/aug-cc-pCVQZ energies.

All the *ab initio* computations up to CCSD(T) are performed using the MOLPRO³⁰ program package. For the CCSDT and CCSDT(Q) computations, the MRCC code,³¹ interfaced to MOLPRO, is employed.

The Hartree–Fock energies, E_n^{HF} , are extrapolated to the CBS limit, $E_{\text{CBS}}^{\text{HF}}$, using³²

$$E_n^{\text{HF}} = E_{\text{CBS}}^{\text{HF}} + a(n+1)e^{-9\sqrt{n}}. \quad (1)$$

For the all-electron MP2, CCSD, and CCSD(T) correlation energy increments, $E_n^{\text{corr.}}$, the CBS limits, $E_{\text{CBS}}^{\text{corr.}}$, are obtained by the extrapolation formula,³³

$$E_n^{\text{corr.}} = E_{\text{CBS}}^{\text{corr.}} + bn^{-3}. \quad (2)$$

In order to get the best estimates for the CBS limits using the above two-parameter asymptotic formulas, the best two energies, i.e., $n = 4$ and 5 , are used in the extrapolations.

The final FPA classical relative energies are obtained as $\text{HF/CBS} + \delta[\text{MP2}]/\text{CBS} + \delta[\text{CCSD}]/\text{CBS} + \delta[\text{CCSD(T)}]/\text{CBS} + \delta[\text{CCSDT}] + \delta[\text{CCSDT(Q)}] + \Delta_{\text{rel}}$, where symbol δ denotes the correlation energy increments with respect to the preceding level of theory. The ground-state vibrationally adiabatic relative energies are calculated by adding the harmonic zero-point energy (ZPE) corrections to the above classical values.

B. Structures and relative energies of the stationary points

The different reaction pathways and the corresponding stationary points on the PES of the $\text{F}^- + \text{CH}_3\text{F}$ reaction are shown in Figure 1. The double-well potential profile of the back-side attack Walden inversion is symmetric with respect to the central transition state (TS2 in Fig. 1) of D_{3h} point-group symmetry. The saddle-point energy is just slightly below the reactant asymptote, whereas the wells are as deep as $13\text{--}14 \text{ kcal mol}^{-1}$. In the wells, we have found a C_{3v} ion-dipole complex (MIN2) and a C_s hydrogen-bonded (H-bonded) complex (MIN1) with similar energy separated by a C_s saddle-point (TS1) which is just above the minima by about $0.5 \text{ kcal mol}^{-1}$. Note that similar H-bonded entrance-channel complexes were found for the $\text{F}^- + \text{CH}_3\text{Cl}$ (Refs. 11 and 12) and $\text{F}^- + \text{CH}_3\text{I}$ (Refs. 34 and 35) reactions. However, in the case of $\text{Y} = \text{Cl}$ and I , the H-bonded minimum was significantly deeper than the C_{3v} ion-dipole minimum, whereas for the $\text{F}^- + \text{CH}_3\text{F}$ reaction, the two complexes have the same energy within $0.1 \text{ kcal mol}^{-1}$. As also shown in Figure 1, the front-side attack retention pathway goes through a high barrier of about 46 kcal mol^{-1} and the corresponding saddle-point (TS5) has C_s symmetry where one H atom and the C atom are in the C_s plane and the other two H atoms and the two F atoms are out of the plane. It is interesting to note that in the case of the C_s front-side attack saddle-point geometry of $\text{F}^- + \text{CH}_3\text{Cl}$, four atoms, H, C, F, Cl, are in the C_s plane.^{12,13} The double-inversion classical barrier height (see TS4 in Fig. 1) of about 29 kcal mol^{-1} is substantially lower than that of the front-side attack. The proton-abstraction channel leading to $\text{HF} + \text{CH}_2\text{F}^-$ opens at around 40 kcal mol^{-1} ,

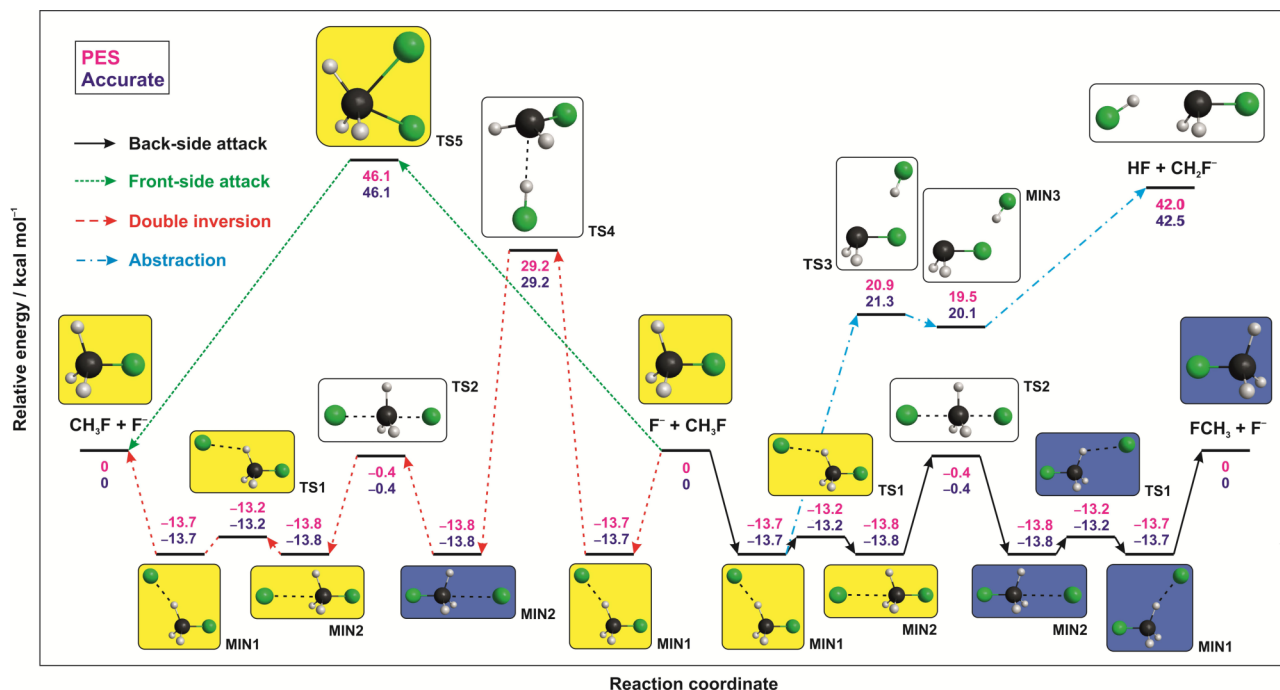


FIG. 1. Schematic energy diagram of the $F^- + CH_3F$ reaction showing the stationary points and the different stereo-specific reaction pathways leading to retention (yellow) and inversion (blue) of the initial configuration (yellow). The accurate benchmark energies (focal-point data, see Tables I–IV) and those corresponding to the analytical PES are relative to the $F^- + CH_3F$ (eq) asymptote.

well above the double-inversion barrier and slightly below the front-side attack saddle point. As seen in Figure 1, the highly endothermic proton abstraction pathway is barrierless featuring a saddle point (TS3) and a minimum (MIN3) at around 20 kcal mol^{-1} above the reactant asymptote.

The benchmark FPA^{19,20} classical relative energies of the above-mentioned stationary points are given in Tables I–III and a summary of the FPA results including ZPE-corrected adiabatic energies is given in Table IV. As Table I shows, electron correlation plays an important role in the accurate determination of the Walden inversion barrier height. The HF method gives a substantial positive barrier, $8.60 \text{ kcal mol}^{-1}$, MP2 decreases the HF barrier height by $7.75 \text{ kcal mol}^{-1}$, CCSD increases the MP2 value by $1.65 \text{ kcal mol}^{-1}$, and CCSD(T) decreases the CCSD result by $2.63 \text{ kcal mol}^{-1}$, resulting in a slightly negative CCSD(T)/CBS barrier height of $-0.13 \text{ kcal mol}^{-1}$. The $\delta[\text{CCSDT}]$ and $\delta[\text{CCSDT}(\text{Q})]$ correlation effects further decrease the barrier height by 0.13 and $0.14 \text{ kcal mol}^{-1}$, respectively, resulting in a $-0.39 \text{ kcal mol}^{-1}$ value. After adding the $\Delta_{\text{rel}} = -0.06 \text{ kcal mol}^{-1}$ correction, we arrive to our best estimate of the classical central barrier height of $-0.45 \pm 0.10 \text{ kcal mol}^{-1}$, where the uncertainty is estimated based on the data of Table I. The adiabatic barrier height of $-0.61 \pm 0.10 \text{ kcal mol}^{-1}$ is slightly deeper, because the ZPE correction, $-0.16 \text{ kcal mol}^{-1}$, decreases the barrier as shown in Table IV. The final FPA classical(adiabatic) energies for the C_{3v} and C_s minima and the saddle point between them are $-13.81(-13.56)$ and $-13.73(-13.52)$ and $-13.21(-13.15) \text{ kcal mol}^{-1}$, respectively, relative to the reactant asymptote. As Tables I and IV show the HF method gives $2\text{--}3 \text{ kcal mol}^{-1}$ shallower well, the MP2 method decreases the depth by about 2 kcal mol^{-1} , and the correlation effects beyond MP2 are about $-0.5 \text{ kcal mol}^{-1}$. Since both the $\delta[\text{CCSDT}(\text{Q})]$

and Δ_{rel} contributions are $0.00 \text{ kcal mol}^{-1}$, the final FPA electronic energy is converged to the relativistic all-electron full configuration interaction limit. Furthermore, on the basis of Table I, the extrapolated CBS results are converged with respect to the basis size within $\pm 0.05 \text{ kcal mol}^{-1}$, which is our estimated uncertainty for the above well depths.

Table II shows the FPA results for the proton-abstraction channel. The best estimate for the classical endothermicity is $42.54 \pm 0.10 \text{ kcal mol}^{-1}$, which is significantly reduced by the ZPE correction of $-4.42 \text{ kcal mol}^{-1}$, resulting in a 0 K reaction enthalpy of $38.1 \pm 0.2 \text{ kcal mol}^{-1}$. The classical FPA result is well converged with respect to the electron correlation treatment and the uncertainty comes from that of the $\delta[\text{MP2}]/\text{CBS}$ increment (see Table II). The uncertainty of the adiabatic value is mainly due to the uncertainty of the ZPE correction, which could be improved by considering vibrational anharmonicity. The HF method overestimates the relative energies of the saddle point and minimum along the abstraction pathway by about 3 kcal mol^{-1} . The final classical(adiabatic) FPA values are $21.28(18.60)$ and $20.10(17.85) \text{ kcal mol}^{-1}$ for the saddle point and minimum, respectively. As seen, the ZPE corrections are substantial for the above relative energies as well and their uncertainties are similar to those of the reaction enthalpy.

The FPA results for the front-side attack and double-inversion classical barrier heights are given in Table III and the ZPE-corrected adiabatic results are shown in Table IV. Similar to the central transition state, electron correlation significantly affects the barrier heights. The CBS limits of the HF, MP2, CCSD, CCSD(T), CCSDT, and CCSDT(Q) front-side attack classical barrier heights are 65.43 , 47.42 , 51.50 , 46.69 , 46.52 , and $46.16 \text{ kcal mol}^{-1}$, respectively, and the corresponding values for the double inversion are 38.19 , 29.91 , 30.75 , 29.30 , 29.29 , and $29.17 \text{ kcal mol}^{-1}$. In both cases, the HF method

TABLE I. Focal-point analysis of the classical energies (in kcal mol⁻¹) of the substitution-channel saddle points and complexes relative to the reactant asymptote energy.^a

$[F \cdots CH_3 \cdots F]_{TS2}^-$	HF	δ [MP2]	δ [CCSD]	δ [CCSD(T)]	δ [CCSDT] ^b	δ [CCSDT(Q)] ^b	V_{TS2}
aug-cc-pCVDZ	5.60	-7.90	+1.20	-2.47	-0.13	-0.14	-3.84
aug-cc-pCVTZ	8.30	-7.82	+1.44	-2.65	[-0.13]	[-0.14]	-1.00
aug-cc-pCVQZ	8.49	-7.90	+1.54	-2.64	[-0.13]	[-0.14]	-0.78
aug-cc-pCV5Z	8.58	-7.83	+1.59	-2.63	[-0.13]	[-0.14]	-0.55
CBS ^c	8.60	-7.75	+1.65	-2.63	-0.13	-0.14	-0.39
$V_{TS2}(\text{final}) = V_{TS2}(\text{AE-CCSDT(Q)/CBS}) + \Delta_{\text{rel}} = -0.39 - 0.06 = \mathbf{-0.45}$							
$[F^- \cdots H_3CF]_{MIN2}$	HF	δ [MP2]	δ [CCSD]	δ [CCSD(T)]	δ [CCSDT] ^b	δ [CCSDT(Q)] ^b	V_{MIN2}
aug-cc-pCVDZ	-12.41	-1.56	-0.21	-0.47	-0.03	+0.00	-14.69
aug-cc-pCVTZ	-11.68	-1.71	-0.21	-0.44	[-0.03]	[+0.00]	-14.07
aug-cc-pCVQZ	-11.60	-1.72	-0.21	-0.41	[-0.03]	[+0.00]	-13.97
aug-cc-pCV5Z	-11.56	-1.68	-0.20	-0.40	[-0.03]	[+0.00]	-13.88
CBS ^c	-11.56	-1.64	-0.19	-0.39	-0.03	0.00	-13.81
$V_{MIN2}(\text{final}) = V_{MIN2}(\text{AE-CCSDT(Q)/CBS}) + \Delta_{\text{rel}} = -13.81 + 0.00 = \mathbf{-13.81}$							
$[F^- \cdots HCH_2F]_{MIN1}$	HF	δ [MP2]	δ [CCSD]	δ [CCSD(T)]	δ [CCSDT] ^b	δ [CCSDT(Q)] ^b	V_{MIN1}
aug-cc-pCVDZ	-11.67	-2.23	-0.12	-0.57	-0.04	+0.00	-14.61
aug-cc-pCVTZ	-11.01	-2.38	-0.10	-0.51	[-0.04]	[+0.00]	-14.04
aug-cc-pCVQZ	-10.96	-2.40	-0.07	-0.48	[-0.04]	[+0.00]	-13.94
aug-cc-pCV5Z	-10.93	-2.34	-0.06	-0.47	[-0.04]	[+0.00]	-13.82
CBS ^c	-10.92	-2.28	-0.04	-0.45	-0.04	+0.00	-13.73
$V_{MIN1}(\text{final}) = V_{MIN1}(\text{AE-CCSDT(Q)/CBS}) + \Delta_{\text{rel}} = -13.73 + 0.00 = \mathbf{-13.73}$							
$[F^- \cdots HCH_2F]_{TS1}$	HF	δ [MP2]	δ [CCSD]	δ [CCSD(T)]	δ [CCSDT] ^b	δ [CCSDT(Q)] ^b	V_{TS1}
aug-cc-pCVDZ	-11.71	-1.59	-0.18	-0.46	-0.04	+0.00	-13.97
aug-cc-pCVTZ	-11.06	-1.77	-0.18	-0.43	[-0.04]	[+0.00]	-13.47
aug-cc-pCVQZ	-10.99	-1.78	-0.16	-0.40	[-0.04]	[+0.00]	-13.37
aug-cc-pCV5Z	-10.96	-1.74	-0.15	-0.38	[-0.04]	[+0.00]	-13.28
CBS ^c	-10.96	-1.71	-0.14	-0.37	-0.04	+0.00	-13.21
$V_{TS1}(\text{final}) = V_{TS1}(\text{AE-CCSDT(Q)/CBS}) + \Delta_{\text{rel}} = -13.21 + 0.00 = \mathbf{-13.21}$							

^aThe energies correspond to the structures optimized at the all-electron CCSD(T)-F12b/cc-pCVTZ-F12 level of theory. The symbol δ denotes the increments with respect to the preceding level of theory. Brackets signify assumed, non-extrapolated increments from smaller basis sets. The bold numbers are the final FPA results with and without relativistic corrections (Δ_{rel}).

^bEnergy increments obtained from frozen-core CCSD(T), CCSDT, and CCSDT(Q) computations with the aug-cc-pVDZ basis.

^cThe CBS HF energy and the MP2, CCSD, and CCSD(T) electron correlation energy increments were computed using the two-parameter extrapolation formulas given in Eqs. (1) and (2), respectively. Only the energies corresponding to aug-cc-pCVnZ [$n = Q(4)$ and 5] were included in the extrapolations.

seriously overestimates the barrier heights, MP2 provides reasonable results, and CCSD is worse than MP2. The T_1 diagnostic³⁶ values, which show the multi-reference character of the wavefunctions, are 0.018 and 0.011 for the front-side attack and double-inversion saddle points, respectively. This suggests that even the front-side attack barrier height can be computed by a single-reference method (T_1 value is less than 0.020). The δ [CCSDT(Q)] increment of -0.36 kcal mol⁻¹ indicates that the electron correlation effects beyond CCSDT(Q) are as little as about -0.1 kcal mol⁻¹ for the front-side attack barrier height. Applying the scalar relativistic corrections, we get our final estimates of 46.07 ± 0.20 and 29.18 ± 0.20 kcal mol⁻¹ for the front-side attack and double-inversion classical barrier heights, respectively. The ZPE correction decreases the former value by 0.92 kcal mol⁻¹ and the latter by 3.11 kcal mol⁻¹, resulting in adiabatic barrier heights of 45.16 ± 0.30 and 26.07 ± 0.30 kcal mol⁻¹, respectively. The uncertainties are estimated considering the accuracy of the CBS extrapolations

and the effects of the higher-order excitations (based on Table III) as well as the uncertainty of the ZPE correction.

The accurate structural parameters and harmonic frequencies of the stationary points are given in Tables V–VIII. Along the Walden inversion pathway, the CH bond length does not change significantly; it varies between 1.069 Å (central TS) and 1.107 Å (H-bonded complex), whereas the equilibrium value for CH₃F is 1.087 Å. On the basis of the CH stretching fundamentals, the H-bonded complex can be identified, because the H-bonded CH stretching frequency is only 2824 cm⁻¹, red-shifted significantly by 225 cm⁻¹ relative to the symmetric stretching mode of CH₃F (3049 cm⁻¹). For $[F^- \cdots HCH_2F]_{TS1}$, $[F^- \cdots H_3CF]_{MIN2}$, and $[F \cdots CH_3 \cdots F]_{TS2}^-$, a slight blue-shift is seen, since the CH frequencies are 3059 , 3112 , and 3163 cm⁻¹, respectively. The increasing frequencies are consistent with the decreasing CH bond lengths, 1.085 , 1.081 , and 1.069 Å, in order, because the shorter bond lengths mean stronger bonds, i.e., larger force constants, thus

TABLE II. Focal-point analysis of the classical energies (in kcal mol⁻¹) of the abstraction-channel saddle point, complex, and reaction heat relative to the reactant asymptote energy.^a

[FH...CH ₂ F ⁻] _{TS3}	HF	δ[MP2]	δ[CCSD]	δ[CCSD(T)]	δ[CCSDT] ^b	δ[CCSDT(Q)] ^b	V _{TS3}
aug-cc-pCVDZ	24.60	-1.54	-2.01	-1.02	-0.04	-0.05	19.95
aug-cc-pCVTZ	24.88	-1.57	-1.84	-0.85	[-0.04]	[-0.05]	20.54
aug-cc-pCVQZ	24.72	-1.38	-1.74	-0.79	[-0.04]	[-0.05]	20.73
aug-cc-pCV5Z	24.74	-1.14	-1.73	-0.76	[-0.04]	[-0.05]	21.02
CBS ^c	24.75	-0.90	-1.72	-0.74	-0.04	-0.05	21.31
$V_{TS3}(\text{final}) = V_{TS3}(\text{AE-CCSDT(Q)/CBS}) + \Delta_{\text{rel}} = 21.31 - 0.03 = \mathbf{21.28}$							
[FH...CH ₂ F ⁻] _{MIN3}	HF	δ[MP2]	δ[CCSD]	δ[CCSD(T)]	δ[CCSDT] ^b	δ[CCSDT(Q)] ^b	V _{MIN3}
aug-cc-pCVDZ	23.11	-1.41	-2.13	-1.05	-0.03	-0.04	18.44
aug-cc-pCVTZ	23.28	-1.26	-1.96	-0.84	[-0.03]	[-0.04]	19.15
aug-cc-pCVQZ	23.14	-1.00	-1.86	-0.77	[-0.03]	[-0.04]	19.44
aug-cc-pCV5Z	23.19	-0.73	-1.85	-0.75	[-0.03]	[-0.04]	19.79
CBS ^c	23.20	-0.45	-1.84	-0.72	-0.03	-0.04	20.12
$V_{MIN3}(\text{final}) = V_{MIN3}(\text{AE-CCSDT(Q)/CBS}) + \Delta_{\text{rel}} = 20.12 - 0.02 = \mathbf{20.10}$							
ΔH	HF	δ[MP2]	δ[CCSD]	δ[CCSD(T)]	δ[CCSDT] ^b	δ[CCSDT(Q)] ^b	ΔH
aug-cc-pCVDZ	44.28	+0.69	-2.22	-0.53	-0.04	-0.04	42.15
aug-cc-pCVTZ	43.87	+0.82	-2.03	-0.35	[-0.04]	[-0.04]	42.23
aug-cc-pCVQZ	43.56	+1.01	-1.95	-0.30	[-0.04]	[-0.04]	42.24
aug-cc-pCV5Z	43.50	+1.19	-1.95	-0.28	[-0.04]	[-0.04]	42.38
CBS ^c	43.49	+1.38	-1.96	-0.26	-0.04	-0.04	42.57
$\Delta H(\text{final}) = \Delta H(\text{AE-CCSDT(Q)/CBS}) + \Delta_{\text{rel}} = 42.57 - 0.04 = \mathbf{42.54}$							

^aThe energies correspond to the structures optimized at the all-electron CCSD(T)-F12b/cc-pCVTZ-F12 level of theory. The symbol δ denotes the increments with respect to the preceding level of theory. Brackets signify assumed, non-extrapolated increments from smaller basis sets. The bold numbers are the final FPA results with and without relativistic corrections (Δ_{rel}).

^bEnergy increments obtained from frozen-core CCSD(T), CCSDT, and CCSDT(Q) computations with the aug-cc-pVDZ basis.

^cThe CBS HF energy and the MP2, CCSD, and CCSD(T) electron correlation energy increments were computed using the two-parameter extrapolation formulas given in Eqs. (1) and (2), respectively. Only the energies corresponding to aug-cc-pCVnZ [n = Q(4) and 5] were included in the extrapolations.

larger frequencies. In the case of the C_{3v} and C_s minima and the TS1 between them, 9 frequencies correspond to the intra-molecular vibrations of the CH₃F unit, whereas 3 low-frequency intermolecular modes exist. For the C_{3v} complex,

there is an intermolecular stretching mode (180 cm⁻¹) and a doubly degenerate intermolecular bending mode (121 cm⁻¹). For the C_s complexes, the degenerate frequencies split. For TS1, the imaginary frequency is only 106i cm⁻¹. The central

TABLE III. Focal-point analysis of the front-side attack and double-inversion classical barrier heights (in kcal mol⁻¹) relative to the reactant asymptote energy.^a

[FFCH ₃] ⁻ _{TS5}	HF	δ[MP2]	δ[CCSD]	δ[CCSD(T)]	δ[CCSDT] ^b	δ[CCSDT(Q)] ^b	V _{TS5}
aug-cc-pCVDZ	62.62	-18.07	+3.11	-4.42	-0.18	-0.36	42.72
aug-cc-pCVTZ	65.16	-18.27	+3.70	-4.80	[-0.18]	[-0.36]	45.25
aug-cc-pCVQZ	65.32	-18.20	+3.92	-4.81	[-0.18]	[-0.36]	45.69
aug-cc-pCV5Z	65.41	-18.10	+4.00	-4.81	[-0.18]	[-0.36]	45.96
CBS ^c	65.43	-18.01	+4.08	-4.81	-0.18	-0.36	46.16
$V_{TS5}(\text{final}) = V_{TS5}(\text{AE-CCSDT(Q)/CBS}) + \Delta_{\text{rel}} = 46.16 - 0.08 = \mathbf{46.07}$							
[FH...CH ₂] ⁻ _{TS4}	HF	δ[MP2]	δ[CCSD]	δ[CCSD(T)]	δ[CCSDT] ^b	δ[CCSDT(Q)] ^b	V _{TS4}
aug-cc-pCVDZ	39.04	-7.65	+0.33	-1.50	-0.01	-0.13	30.08
aug-cc-pCVTZ	38.26	-8.52	+0.64	-1.50	[-0.01]	[-0.13]	28.74
aug-cc-pCVQZ	38.18	-8.57	+0.77	-1.47	[-0.01]	[-0.13]	28.77
aug-cc-pCV5Z	38.18	-8.43	+0.81	-1.46	[-0.01]	[-0.13]	28.97
CBS ^c	38.19	-8.27	+0.84	-1.45	-0.01	-0.13	29.17
$V_{TS4}(\text{final}) = V_{TS4}(\text{AE-CCSDT(Q)/CBS}) + \Delta_{\text{rel}} = 29.17 + 0.01 = \mathbf{29.18}$							

^aThe energies correspond to the structures optimized at the all-electron CCSD(T)-F12b/cc-pCVTZ-F12 level of theory. The symbol δ denotes the increments with respect to the preceding level of theory. Brackets signify assumed, non-extrapolated increments from smaller basis sets. The bold numbers are the final FPA results with and without relativistic corrections (Δ_{rel}).

^bEnergy increments obtained from frozen-core CCSD(T), CCSDT, and CCSDT(Q) computations with the aug-cc-pVDZ basis.

^cThe CBS HF energy and the MP2, CCSD, and CCSD(T) electron correlation energy increments were computed using the two-parameter extrapolation formulas given in Eqs. (1) and (2), respectively. Only the energies corresponding to aug-cc-pCVnZ [n = Q(4) and 5] were included in the extrapolations.

TABLE IV. Summary of the FPA relative energies (in kcal mol⁻¹) including the effects of scalar relativity (Rel.) and ZPE for the stationary points of the back-side attack substitution, abstraction, and retention (front-side attack and double inversion) pathways.^a

	Back-side attack substitution			Abstraction			Retention		
	TS2	MIN2	MIN1	TS1	MIN3	TS3	ΔH	TS5	TS4
HF ^b	8.60	-11.56	-10.92	-10.96	23.20	24.75	43.49	65.43	38.19
MP2 ^b	0.84	-13.20	-13.20	-12.67	22.75	23.85	44.87	47.42	29.91
CCSD ^b	2.50	-13.39	-13.24	-12.81	20.91	22.14	42.92	51.50	30.75
CCSD(T) ^b	-0.13	-13.77	-13.69	-13.18	20.19	21.40	42.65	46.69	29.30
CCSDT ^b	-0.25	-13.81	-13.73	-13.21	20.16	21.36	42.61	46.52	29.29
CCSDT(Q) ^b	-0.39	-13.81	-13.73	-13.21	20.12	21.31	42.57	46.16	29.17
$\Delta\text{Rel.}^c$	-0.06	+0.00	+0.00	+0.00	-0.02	-0.03	-0.04	-0.08	+0.01
Final classical	-0.45	-13.81	-13.73	-13.21	20.10	21.28	42.54	46.07	29.18
ΔZPE^d	-0.16	+0.24	+0.21	+0.06	-2.25	-2.68	-4.42	-0.92	-3.11
Final + ΔZPE	-0.61	-13.56	-13.52	-13.15	17.85	18.60	38.11	45.16	26.07

^aThe results correspond to the structures optimized at the AE-CCSD(T)-F12b/cc-pCVTZ-F12 level of theory.^bThe results correspond to the CBS limit.^cRelativistic corrections computed at AE-CCSD(T)/aug-cc-pCVQZ level of theory using Douglas-Kroll one-electron integrals.^dHarmonic ZPE corrections obtained at the FC-CCSD(T)-F12b/cc-pVTZ-F12 level of theory.

transition state (TS2) has a substantial imaginary frequency of 576i cm⁻¹.

The saddle-point and the minimum structure along the proton-abstraction pathway consist of a HF and a CH₂F⁻ unit. The geometry and frequencies of the CH₂F⁻ unit are slightly perturbed relative to the corresponding values in the free CH₂F⁻. Perhaps, the most interesting vibrational mode is the intramolecular HF stretching, which is significantly red-shifted by 558 and 906 cm⁻¹ for [FH...CH₂F⁻]_{TS3} and [FH...CH₂F⁻]_{MIN3}, respectively, relative to the harmonic frequency of the HF molecule (4140 cm⁻¹). This is consistent with the increased FH distances of 0.946 and 0.961 Å, respectively, relative to the bond lengths of the HF molecule (0.917 Å). [FH...CH₂F⁻]_{TS3} is a first-order saddle point with an imaginary frequency of 315i cm⁻¹.

The front-side attack pathway goes through a first-order saddle point with a substantial imaginary frequency of 736i cm⁻¹. The saddle-point geometry has C_s symmetry, the two equivalent CF distances are 1.810 Å, i.e., significantly longer than the CF bond length in the CH₃F molecule (1.382 Å), and the FCF angle is 80.7°. The double inversion also goes through a first-order saddle point which consists of a HF and a CH₂F⁻ group. As seen in Figure 1, the structure of the double-inversion TS is very different from that of the abstraction minimum and saddle point. The double-inversion TS has a substantial imaginary frequency of 949i cm⁻¹, about three times larger than that of the abstraction TS. At the double-inversion TS, the CH₂F⁻ group is almost planar with a HCF angle of 113.4°, whereas the abstraction TS has a trigonal pyramidal CH₂F⁻ group with HCF angle of 100.8°.

TABLE V. Structures and relative energies of the stationary points of the PES.^a

[F...CH ₃ ...F] _{TS2} ⁻		[F _b ⁻ ...H ₃ CF _a] _{MIN2}		[F _b ⁻ ...H _b CH ₂ F _a] _{MIN1}		[F _b ⁻ ...H _b CH ₂ F] _{TS1}					
PES	Accurate ^b	PES	Accurate ^b	PES	Accurate ^b	PES	Accurate ^b				
Structures (Å and degrees)											
<i>r</i> (CF)	1.823	1.820	<i>r</i> (CF _a)	1.430	1.427	<i>r</i> (CF _a)	1.416	1.413	<i>r</i> (CF _a)	1.421	1.418
<i>r</i> (CH)	1.071	1.069	<i>r</i> (CF _b)	2.553	2.561	<i>r</i> (CH _b)	1.106	1.107	<i>r</i> (CH _b)	1.085	1.085
α (HCF)	90.0	90.0	<i>r</i> (CH)	1.082	1.081	<i>r</i> (H _b F _b)	1.763	1.762	<i>r</i> (H _b F _b)	2.014	2.017
			α (HCF _a)	108.7	108.8	α (H _b CF _a)	112.1	112.5	α (H _b CF _a)	112.4	112.6
Relative energies (kcal mol ⁻¹)											
	-0.42	-0.45		-13.75	-13.81		-13.71	-13.73		-13.15	-13.21
[F _b H _b ...CH ₂ F _a] _{MIN3} ⁻		[F _b H _b ...CH ₂ F _a] _{TS3} ⁻		[FFCH ₃] _{TS5} ⁻		[F _b H _b ...CH ₂ F _a] _{TS4} ⁻					
PES	Accurate ^b	PES	Accurate ^b	PES	Accurate ^b	PES	Accurate ^b				
Structures (Å and degrees)											
<i>r</i> (CF _a)	1.558	1.550	<i>r</i> (CF _a)	1.530	1.527	<i>r</i> (CF)	1.813	1.810	<i>r</i> (CF _a)	1.431	1.431
<i>r</i> (CH _b)	2.495	2.570	<i>r</i> (CH _b)	2.169	2.209	<i>r</i> (CH _b)	1.080	1.079	<i>r</i> (CH _b)	1.776	1.766
<i>r</i> (H _b F _b)	0.963	0.961	<i>r</i> (H _b F _b)	0.945	0.946	α (FCF)	80.6	80.7	<i>r</i> (H _b F _b)	1.008	1.006
α (HCF _a)	98.7	99.0	α (HCF _a)	100.5	100.8				α (HCF _a)	113.6	113.4
Relative energies (kcal mol ⁻¹)											
	19.46	20.10		20.91	21.28		46.12	46.07		29.19	29.18

^aSee Fig. 1 for the structures. H_b denotes the H atom in the σ_h plane corresponding to the structures of C_s symmetry.^bAccurate structures are obtained at the AE-CCSD(T)-F12b/cc-pCVTZ-F12 level of theory and the relative energies are the relativistic AE-CCSDT(Q)/CBS quality FPA data.

TABLE VI. Structures and relative energies for the reactants and products on the PES.

F ⁻ + CH ₃ F			HF + CH ₂ F ⁻		
PES	Accurate ^a		PES	Accurate ^a	
Structures (Å and deg)					
<i>r</i> (CF)	1.385	1.382	<i>r</i> (CF)	1.493	1.491
<i>r</i> (CH)	1.088	1.087	<i>r</i> (CH)	1.112	1.110
<i>α</i> (HCF)	108.7	108.8	<i>r</i> (HF)	0.918	0.917
			<i>α</i> (HCF)	101.9	102.0
Relative energies (kcal mol ⁻¹)					
	0	0		42.04	42.54

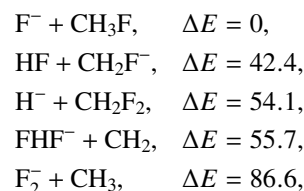
^aAccurate structures are obtained at the AE-CCSD(T)-F12b/cc-pCVTZ-F12 level of theory and the relative energies are the relativistic AE-CCSDT(Q)/CBS quality FPA data.

close to the corresponding angle in the free CH₂F⁻ (102.0°). The HF distance at the double-inversion TS is 1.006 Å, i.e., significantly stretched relative to the bond length of the HF molecule (0.917 Å) and longer than the corresponding values at the abstraction TS and minimum. The longer bond length, i.e., the weaker bond, results in a significant red-shift by 1811 cm⁻¹ of the HF intramolecular frequency.

III. GLOBAL ANALYTICAL *AB INITIO* POTENTIAL ENERGY SURFACE

A. *Ab initio* data and fitting

We develop a global full-dimensional analytical PES for the F⁻ + CH₃F reaction by fitting 49 166 *ab initio* energy points obtained by an efficient composite method. In order to develop a global PES, we have considered the following product channels of the F⁻ + CH₃F reaction:



where the classical endothermicities (ΔE), obtained at the AE-CCSD(T)-F12b/cc-pCVTZ-F12 level of theory, are given in kcal mol⁻¹. All the other possible product channels, e.g., F₂ + CH₃⁻ and F⁻ + HF + CH₂, have significantly higher energies than the above ones. Our goal is to develop a PES, which describes both the halogen-substitution and proton-abstraction channels as well as the front-side attack and double-inversion pathways via barriers of about 46 and 29 kcal mol⁻¹,

TABLE VII. Harmonic vibrational frequencies (in cm⁻¹) for the saddle points and complexes.

	[F⋯CH ₃ ⋯F] _{TS2} ⁻		[F ⁻ ⋯H ₃ CF] _{MIN2}		[F ⁻ ⋯HCH ₂ F] _{MIN1}		[F ⁻ ⋯HCH ₂ F] _{TS1}	
	PES	Accurate ^a	PES	Accurate ^a	PES	Accurate ^a	PES	Accurate ^a
ZPE	8615	8610	8777	8751	8751	8739	8710	8686
1	566 <i>i</i>	576 <i>i</i>	124	121	98	102	103 <i>i</i>	106 <i>i</i>
2	346	344	124	121	235	231	148	146
3	346	344	187	180	248	254	193	186
4	363	374	916	915	978	975	956	956
5	1131	1110	1125	1129	1173	1177	1088	1088
6	1131	1110	1125	1129	1214	1211	1180	1181
7	1230	1247	1386	1387	1482	1489	1417	1421
8	1411	1408	1501	1482	1521	1519	1505	1491
9	1411	1408	1501	1482	1556	1551	1530	1509
10	3165	3163	3114	3112	2846	2824	3061	3059
11	3348	3356	3224	3221	3066	3055	3146	3155
12	3348	3356	3224	3221	3083	3092	3195	3181
	[FH⋯CH ₂ F ⁻] _{MIN3}		[FH⋯CH ₂ F ⁻] _{TS3}		[FFCH ₃] _{TS5} ⁻		[FH⋯CH ₂ F ⁻] _{TS4}	
	PES	Accurate ^a	PES	Accurate ^a	PES	Accurate ^a	PES	Accurate ^a
ZPE	7980	7879	7756	7729	8337	8346	7518	7580
1	75	62	338 <i>i</i>	315 <i>i</i>	720 <i>i</i>	736 <i>i</i>	959 <i>i</i>	949 <i>i</i>
2	119	105	149	127	247	231	105	100
3	306	317	229	228	301	330	329	302
4	621	616	478	453	595	586	343	368
5	974	961	732	728	1012	982	951	942
6	991	968	785	845	1079	1110	982	1033
7	1222	1161	1190	1147	1312	1320	1077	1108
8	1229	1176	1215	1179	1423	1436	1101	1112
9	1458	1407	1450	1413	1557	1541	1400	1403
10	2852	2845	2850	2849	2965	2970	2341	2329
11	2903	2906	2889	2907	2975	2988	3090	3151
12	3210	3234	3546	3582	3207	3197	3317	3312

^aAccurate results obtained at FC-CCSD(T)-F12b/cc-pVTZ-F12 level of theory.

TABLE VIII. Harmonic vibrational frequencies (in cm^{-1}) for reactant and products.

	CH_3F		CH_2F^-			HF		
	PES	Accurate ^a		PES	Accurate ^a		PES	Accurate ^a
ZPE	8686	8667	ZPE	5086	5050	ZPE	2059	2070
$\omega_3(a_1)$	1072	1075				ω_1	4118	4140
$\omega_6(e)$	1203	1207	$\omega_6(a'')$	721	731			
			$\omega_3(a')$	1150	1112			
$\omega_2(a_1)$	1505	1494	$\omega_5(a'')$	1234	1196			
$\omega_5(e)$	1515	1510	$\omega_2(a')$	1453	1410			
			$\omega_1(a')$	2778	2796			
$\omega_1(a_1)$	3051	3049	$\omega_4(a'')$	2836	2855			
$\omega_4(e)$	3154	3141						

^aAccurate results obtained at FC-CCSD(T)-F12b/cc-pVTZ-F12 level of theory.

respectively. Therefore, we have selected about 30 000 configurations for the FCH_3F^- complex region (defined as $r_{\text{C-F}} < 4 \text{ \AA}$, excluding $\text{H}^- + \text{CH}_2\text{F}_2$ data) and 2182, 2279, 500, and 500 points for the $\text{F}^- + \text{CH}_3\text{F}$, $\text{HF} + \text{CH}_2\text{F}^-$, $\text{H}^- + \text{CH}_2\text{F}_2$, and $\text{FHF}^- + \text{CH}_2$ channels, respectively. In order to describe the long-range ion-dipole interactions, the configuration space is covered up to ion-molecule separations of about 11 \AA , resulting in about 13 000 points at C-F distances larger than 4 \AA (not including the fragment channel configurations).

Following recommendations of the FPA technique,^{19,20} the composite energies are computed as CCSD(T)-F12a/cc-pVDZ-F12 + MP2-F12/cc-pVTZ-F12 – MP2-F12/cc-pVDZ-F12 employing the MOLPRO program package. Test computations at 15 geometries showed that this composite method provides AE-CCSD(T)-F12b/cc-pCVQZ-F12 quality results within a root-mean-square (RMS) error of 0.33 kcal mol^{-1} .³⁷ For comparison, the RMS errors of CCSD(T) with aug-cc-pVDZ, aug-cc-pVTZ, and aug-cc-pVQZ basis sets are 4.01, 1.00, and 0.59 kcal mol^{-1} , respectively, relative to AE-CCSD(T)-F12b/cc-pCVQZ-F12.³⁷

We carry out a 6th-order fit using the permutationally invariant polynomial approach^{38,17} based on Morse-like variables, $\exp(-r_{ij}/a)$, where r_{ij} are the inter-atomic distances, and after some careful investigation, the choice of $a = 3$ bohrs is made. By a weighted linear least-squares fit using weights of $E_0/(E + E_0)$, where $E_0 = 31 \text{ kcal mol}^{-1}$ and energy E is relative to the global minimum, 5850 coefficients are obtained. The RMS fitting errors are remarkably small, 0.15, 0.34, and 0.92 kcal mol^{-1} for the energy ranges 0–31, 31–63, and 63–157 kcal mol^{-1} , respectively. Considering these RMS fitting errors and the accuracy of the composite method, we can conclude that the analytical PES may have an absolute average accuracy of $\sim 0.5 \text{ kcal mol}^{-1}$ up to about 100 kcal mol^{-1} above the global minimum.

B. The properties and accuracy of the analytical PES

The analytical PES describes all the stationary points and reactions pathways discussed in Sec. II. The comparison of the benchmark FPA relative energies and the PES values are shown in Figure 1. As seen, the PES reproduces the FPA data remarkably, perhaps fortuitously, well, since the FPA and PES relative energies agree within 0.1 kcal mol^{-1} for all the stationary points along the back-side attack, front-side attack, and

double-inversion pathways. The largest deviations are seen for the proton-abstraction channel, where the PES underestimates the relative energy of the saddle point, minimum, and products by 0.4, 0.6, and 0.5 kcal mol^{-1} , respectively. We paid special attention to the accuracy of the long-range ion-dipole interactions. Figure 2 shows one-dimensional cuts of the analytical PES and the corresponding direct *ab initio* curves along the $\text{FCH}_3 \cdots \text{F}^-$ and $\text{FCH}_2^- \cdots \text{HF}$ separations. As seen, the analytical PES smoothly and accurately describes the dissociation of the fragments as we increase the C \cdots F and C \cdots H intermolecular distances, respectively, while keeping the other internal coordinates fixed.

The structures of the stationary points and the harmonic frequencies obtained on the analytical PES are compared to the benchmark values in Tables V–VIII. As seen in Tables V and VI, the agreement between the PES and AE-CCSD(T)-F12b/cc-pCVTZ-F12 structural parameters is excellent. Most of the distances agree within 0.001–0.005 \AA and all the important angles agree within 0.5° or much better. It is impressive that some of the long-range intermolecular distances are also very accurate on the PES. For example, the C \cdots F distances for the central TS, C_{3v} ion-dipole complex, and front-side attack TS are 1.823(1.820), 2.553(2.561), and 1.813(1.810) \AA , respectively, and the F \cdots H distances at H-bonded minimum and TS are 1.763(1.762) and 2.014(2.017) \AA , respectively, where the benchmark results are given in parentheses. As Tables VII and VIII show, the harmonic frequencies of the stationary points corresponding to the PES agree also very well with the benchmark *ab initio* data. The PES values for the imaginary frequencies of the central, front-side attack, and double-inversion saddle points deviate from the benchmark values by only 10, 16, and 10 cm^{-1} , respectively. Many PES and benchmark fundamental frequencies agree within a few cm^{-1} and the RMS deviations are only around 10–30 cm^{-1} for all the stationary points shown in Table VII.

IV. QUASICLASSICAL TRAJECTORY CALCULATIONS

A. Computational details

QCT calculations are performed for the $\text{F}^- + \text{CH}_3\text{F}(v = 0)$ reaction using the new full-dimensional *ab initio* PES. The vibrational ground state ($v = 0$) of CH_3F is prepared by standard normal-mode sampling and the rotational angular

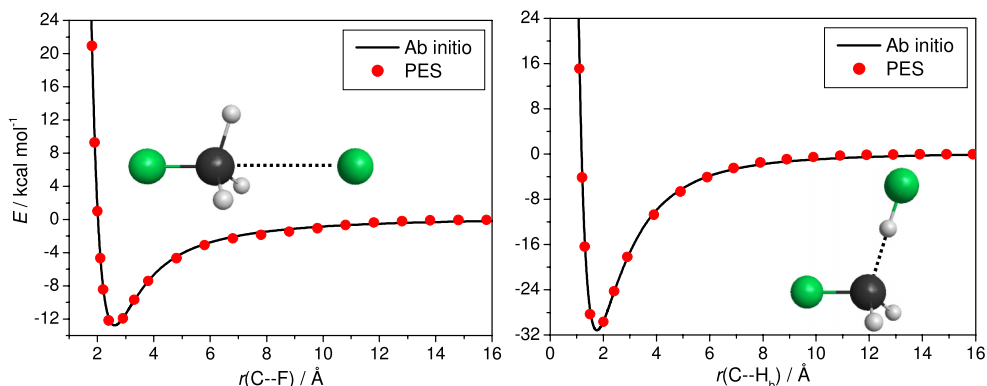


FIG. 2. Potential energy curves for the $F^- + CH_3F \rightarrow CH_3F + F^-$ substitution and $F^- + CH_3F \rightarrow HF + CH_2F^-$ abstraction reactions as a function of the $r(C-F)$ and $r(C-H_b)$ distances, respectively. The $F-C-F$ (substitution) and $C-H_b-F$ (abstraction) atoms are kept collinear along the one-dimensional cuts. The $HF(eq)$ and $CH_3F(eq)$ structures are obtained at the AE-CCSD(T)-F12b/cc-pCVTZ-F12 level of theory, whereas the *ab initio* results were obtained with the composite method. The energies are relative to the $F^- + CH_3F(eq)$ and $HF(eq) + CH_2F^-(eq)$ asymptotes for the substitution and abstraction reactions, respectively.

momentum of CH_3F is set to zero. Trajectories are run at collision energies (E_{coll}) of 1, 2, 4, 7, 10, 15, 20, 30, 40, 50, 60, 70, and 80 kcal mol $^{-1}$. The initial orientation of CH_3F is randomly sampled and the distance of the reactants is $(x^2 + b^2)^{1/2}$, where b is the impact parameter and x is 20 bohrs (25 bohrs at the lowest E_{coll}). b is scanned from 0 to b_{max} with a step size of 0.5 bohrs, except at $E_{coll} = 1$ and 2 kcal mol $^{-1}$, where a step size of 1 bohr is used. In order to get improved statistics for the retention integral cross sections at $E_{coll} = 30-80$ kcal mol $^{-1}$, a much smaller step size of 0.125 bohrs is employed. The maximum b (b_{max}) is found to vary between 22 and 7 bohrs for the E_{coll} range of 1 and 10 kcal mol $^{-1}$, and it has a nearly constant value of ~ 5 bohrs in the E_{coll} range of 15 and 80 kcal mol $^{-1}$. At each b , 5000 trajectories are computed; thus, the total number of trajectories is in the range of 65 000–115 000 at $E_{coll} = 1-20$ kcal mol $^{-1}$ and 245 000 at higher collision energies. The trajectories are propagated using a 0.0726 fs (3 a.u. of time) time step and each trajectory is stopped when the maximum of the actual inter-atomic distances is 1 bohr larger than the initial one.

B. Dynamics

Opacity functions (reaction probabilities *vs.* b) for the substitution (halogen exchange) and abstraction (proton transfer) channels are shown in Figure 3. At low E_{coll} , the b_{max} of the substitution channel is large and decreases rapidly with increasing E_{coll} . At $E_{coll} = 1, 2, 4,$ and 10 kcal mol $^{-1}$, the b_{max} values are about 22, 15, 9, and 7 bohrs, respectively, showing the importance of the long-range attractive ion-dipole interactions, which play significant role in the dynamics at low E_{coll} and diminish as E_{coll} increases. At larger collision energies, the b_{max} is nearly constant around 5 bohrs. The $b = 0$ reaction probabilities also vary with E_{coll} . At $E_{coll} = 1, 2,$ and 4 kcal mol $^{-1}$, $P(b = 0)$ is 6%, 4%, and 2%, respectively. Then, at $E_{coll} = 10$ and 15 , $P(b = 0)$ is as high as 24% and 29%, and at larger E_{coll} in the 50–80 kcal mol $^{-1}$ range, $P(b = 0)$ is around 15%–20%. The substantial increase of $P(b = 0)$ at E_{coll} around 10–15 kcal mol $^{-1}$ may be explained by the fact that the well depth of the PES is about 14 kcal mol $^{-1}$. The b_{max} values of the abstraction are about 5 bohrs without significant E_{coll} dependence. The abstraction probabilities increase with E_{coll} .

At $E_{coll} = 50, 70,$ and 80 kcal mol $^{-1}$, the $P(b = 0)$ values are 0.5%, 1.9%, and 3.4%, respectively.

Excitation functions (integral cross sections *vs.* E_{coll}) are shown for the substitution and abstraction reactions in Figure 4. Without any ZPE constraint, the substitution cross sections decrease rapidly as E_{coll} increases from 1 to 5 kcal mol $^{-1}$, then increase between $E_{coll} = 5$ and 10 kcal mol $^{-1}$, and become almost constant at collision energies larger than 10 kcal mol $^{-1}$. This behavior is significantly different from that of the exci-

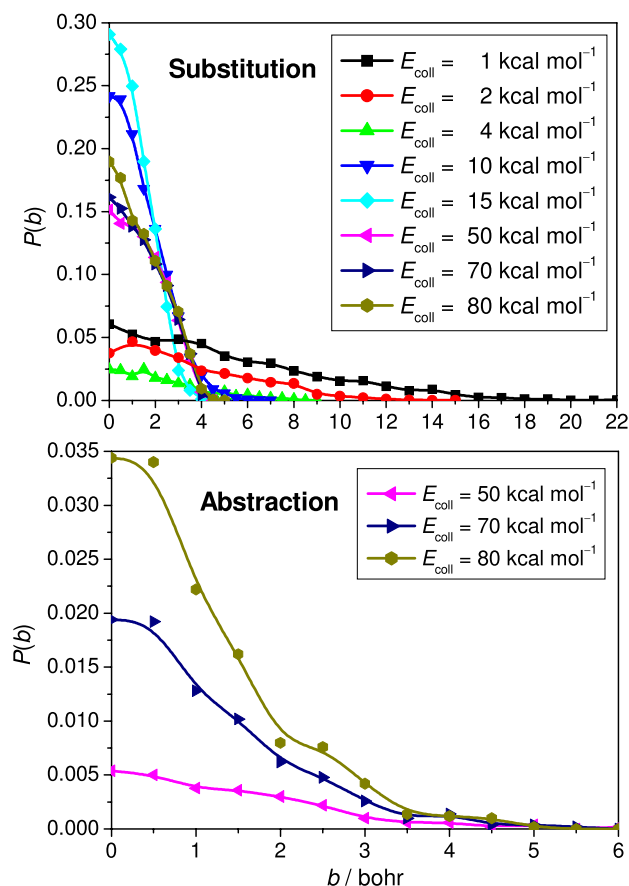


FIG. 3. Reaction probabilities as a function of the impact parameter, b , for the $F^- + CH_3F \rightarrow CH_3F + F^-$ substitution and $F^- + CH_3F \rightarrow HF + CH_2F^-$ abstraction reactions at different collision energies.

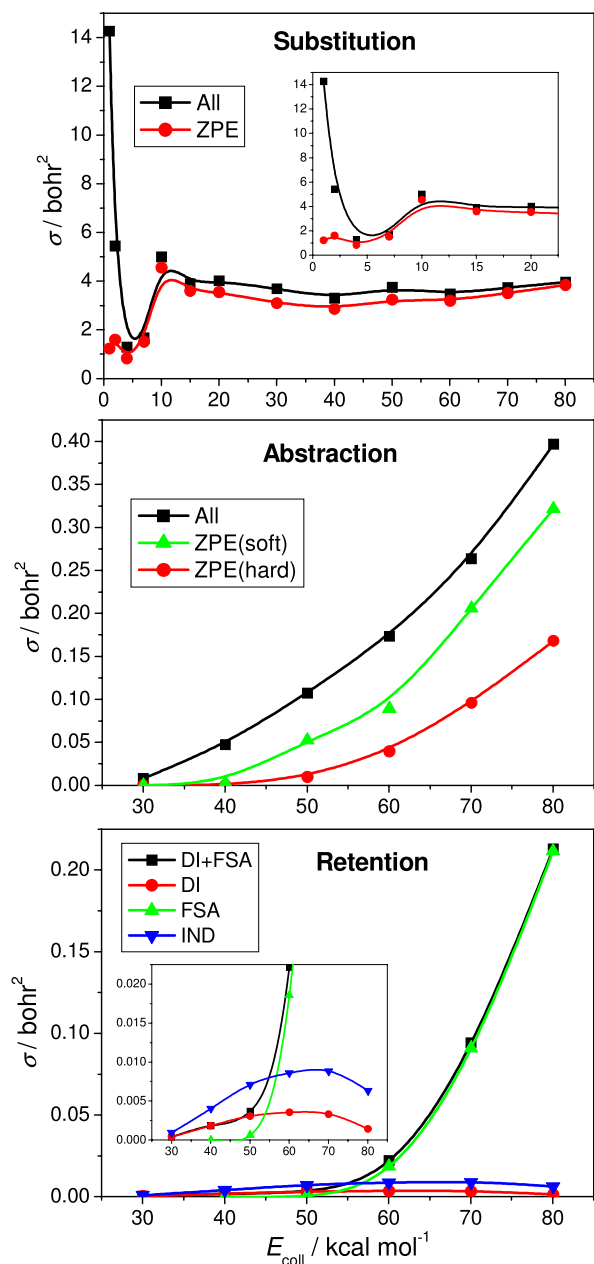


FIG. 4. Integral cross sections as a function of collision energy for the $F^- + \text{CH}_3\text{F} \rightarrow \text{CH}_3\text{F} + F^-$ substitution and $F^- + \text{CH}_3\text{F} \rightarrow \text{HF} + \text{CH}_2\text{F}^-$ abstraction reactions, considering (a) all trajectories (All) without ZPE constraint, (b) ZPE (soft) constraint where trajectories are discarded if the sum of the product vibrational energies is less than the sum of their ZPEs, and (c) ZPE (hard) constraint where trajectories are discarded if either product has less vibrational energy than its ZPE. DI, FSA, and IND denote the double-inversion, front-side attack, and induced-inversion reaction pathways, respectively.

tation function of the exothermic $F^- + \text{CH}_3\text{Cl}$ S_N2 reaction. For $F^- + \text{CH}_3\text{Cl}$, the cross sections monotonically decrease with increasing E_{coll} .^{11,12} For a highly exothermic reaction like $F^- + \text{CH}_3\text{Cl}$, the product ZPE violation is not a concern; however, for the isoenergetic $F^- + \text{CH}_3\text{F}$ S_N2 reaction, the ZPE issue of the QCT method can be serious at low collision energies. Indeed, as Figure 4 shows, the large cross sections of 14.3 and 5.4 bohr² drop to 1.2 and 1.6 bohr² at $E_{\text{coll}} = 1$ and 2 kcal mol⁻¹, respectively, if ZPE constraint is applied to the CH_3F product. At $E_{\text{coll}} = 4$ kcal mol⁻¹, the constrained cross section of 0.8 bohr² is just below the non-constrained

one by 0.5 bohr². At higher E_{coll} , the ZPE violation is only about 10%. Due to the large ZPE effects at low E_{coll} , the shape of ZPE-constrained excitation function is different from that of the non-constrained one. The constrained cross sections are around 1.5 bohr² at low E_{coll} , increase between 7 and 10 kcal mol⁻¹, and become almost constant (around 3.0–3.5 bohr²) at larger E_{coll} (certainly up to 80 kcal mol⁻¹, which is the highest E_{coll} of the present study).

The abstraction reaction is barrier-less and its endothermicity is about 38 kcal mol⁻¹ including ZPE correction; thus, we can expect the occurrence of the $\text{HF} + \text{CH}_2\text{F}^-$ products at collision energies above 38 kcal mol⁻¹. As Figure 4 shows, without ZPE constraint, the threshold of the abstraction channel is only about 30 kcal mol⁻¹ and the excitation function increases rapidly. The non-zero cross sections in the E_{coll} range of 30–38 kcal mol⁻¹ clearly show the ZPE violation issue of the QCT method. In order to get more realistic results, we have applied both the soft and the hard ZPE constraints, in which trajectories are discarded if the sum of the product vibrational energies is less than the sum of their ZPEs (soft) and either product has less vibrational energy than its ZPE (hard). The ZPE constraints do not change the shape of the excitation functions, but shift the threshold to around 38–40 kcal mol⁻¹ (physically correct value) and decrease the cross sections significantly, especially in the case of the hard constraint. At the highest E_{coll} of the present study (80 kcal mol⁻¹), the non-constrained, soft constrained, and hard constrained abstraction cross sections are 0.40, 0.32, and 0.17 bohr², respectively, while the substitution reaction has a cross section of about 4 bohr². Thus, even at high E_{coll} , the substitution reaction dominates. However, due to the fact that the abstraction cross sections increase rapidly with E_{coll} , whereas the substitution reactivity is almost constant, we may expect that the abstraction eventually supersedes substitution as we further increase the collision energy. It is interesting to compare the proton-abstraction excitation functions of the $F^- + \text{CH}_3\text{F}$ and the $F^- + \text{CH}_3\text{Cl}$ reactions. The former has a concave-up shape and increases rapidly (Fig. 4), whereas the latter becomes nearly constant 20 kcal mol⁻¹ above the threshold (Fig. 2 of Ref. 12). Furthermore, the abstraction cross sections of $F^- + \text{CH}_3\text{Cl}$ are about an order of magnitude higher than the $F^- + \text{CH}_3\text{F}$ ones. This finding can be explained by the larger proton affinity of CH_2F^- than that of CH_2Cl^- .

We have identified the retention trajectories using the procedure described in the supplementary material of Ref. 12. We could distinguish between the two different retention mechanisms based on the integration time, because the double inversion is a slow indirect process, whereas the front-side attack is direct and fast. (At $E_{\text{coll}} = 30$ and 40 kcal mol⁻¹, a time limit of 0.65 ps separates the two mechanisms. Interestingly, at $E_{\text{coll}} = 50, 60, 70,$ and 80 kcal mol⁻¹, we have found that longer time limits of 1.5, 1.8, 2.2, and 2.2 ps, respectively, have to be used.) As seen in Figure 4, retention mechanism can occur via the double-inversion mechanism at collision energies above its adiabatic barrier height of ~ 26 kcal mol⁻¹. The front-side attack pathway opens above its barrier height of 45 kcal mol⁻¹ and becomes quickly the dominant retention mechanism as E_{coll} increases. At $E_{\text{coll}} = 60, 70,$ and 80 kcal mol⁻¹, the front-side attack cross sections are 0.02, 0.09, and 0.21 bohr²,

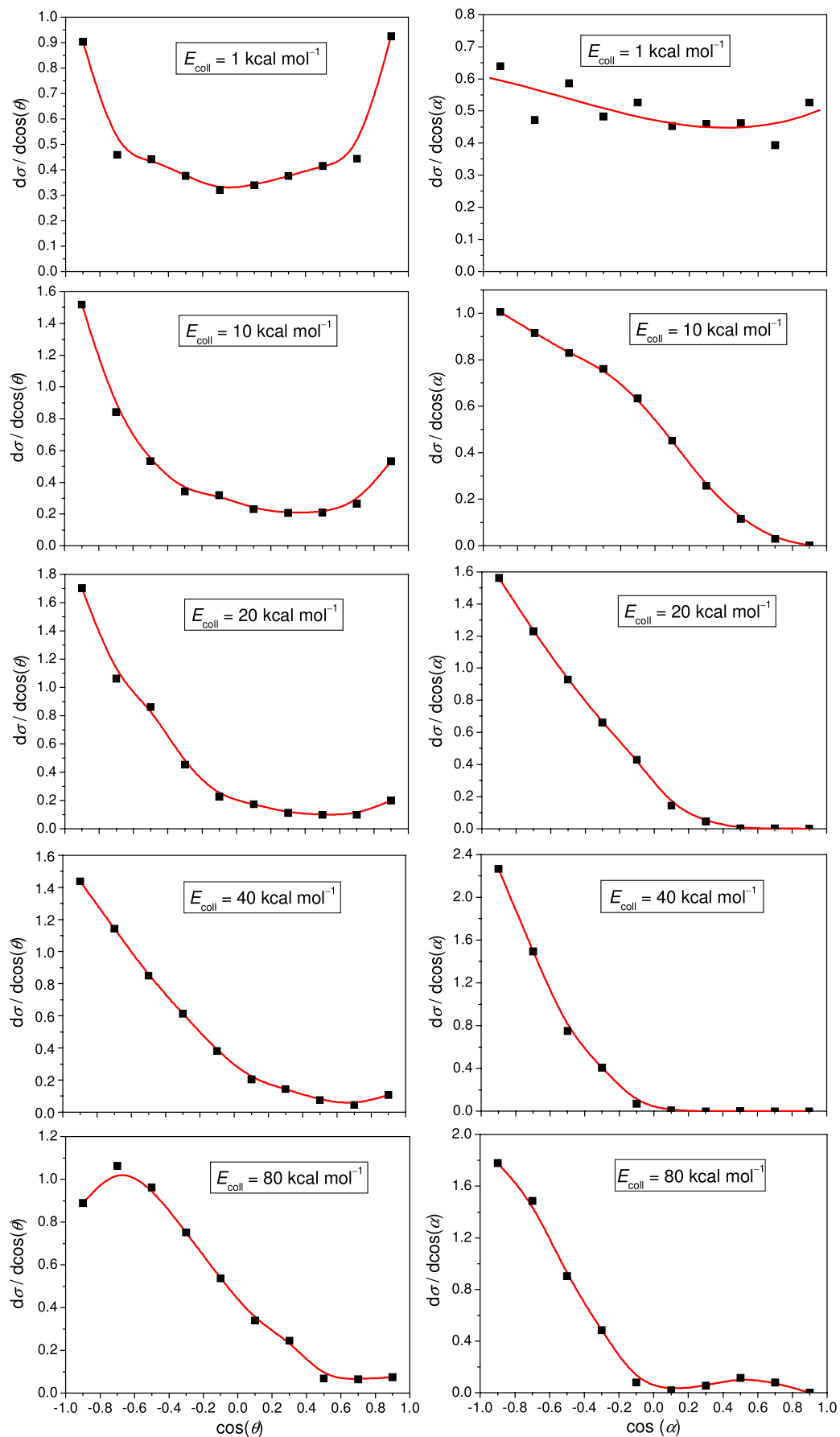


FIG. 5. Scattering angle (left) and initial attack angle (right) distributions at different collision energies for the $F^- + CH_3F$ S_N2 reaction. The scattering angle, θ , is defined as the angle between the initial CH_3F and the final F^- velocity vectors. The attack angle, α , is defined as the angle between the C-F vector and the velocity vector of CH_3F at $t = 0$.

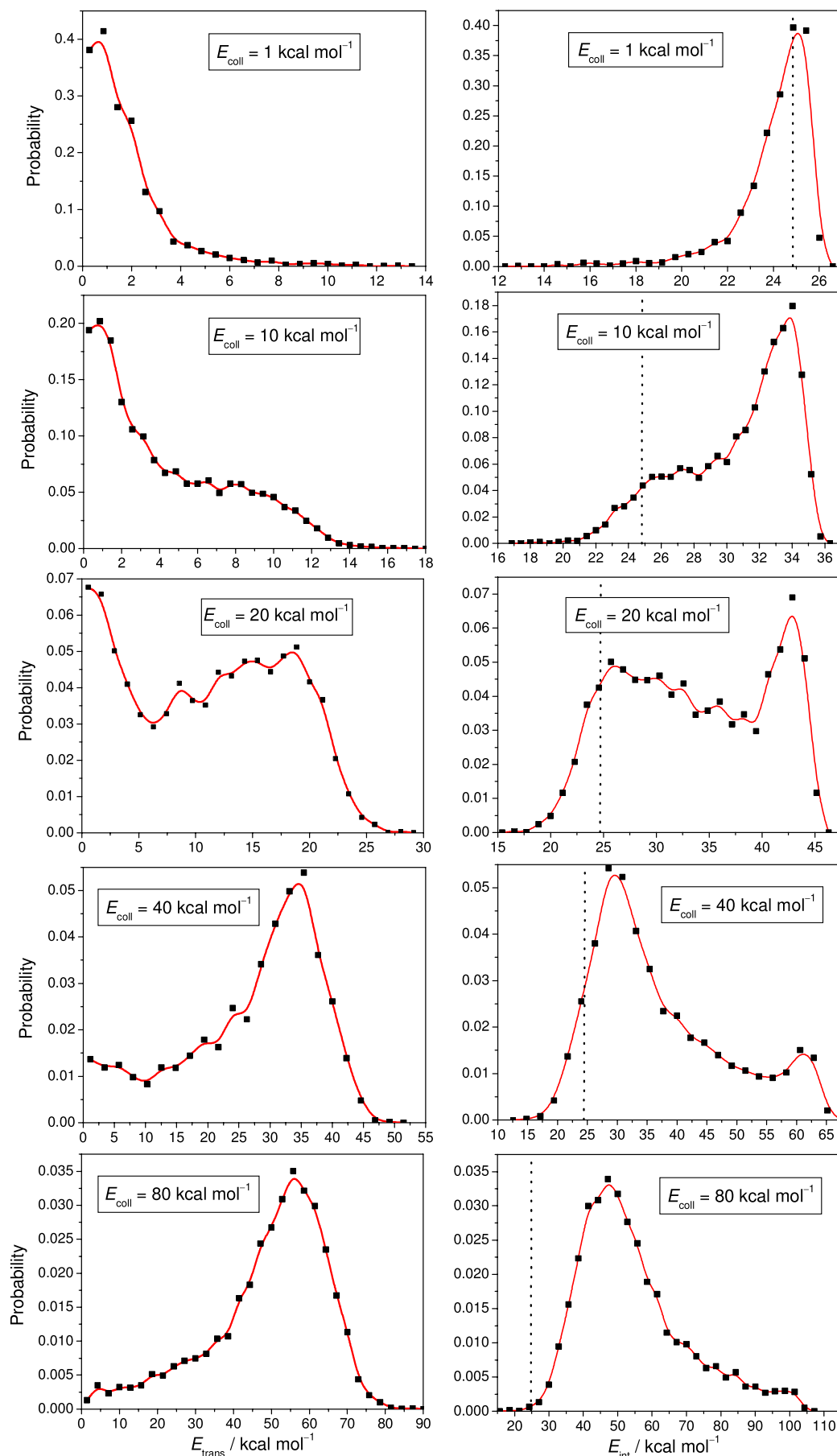


FIG. 6. Product relative translational energy (left) and internal energy (right) distributions at different collision energies for the $\text{F}^- + \text{CH}_3\text{F}$ $\text{S}_{\text{N}}2$ reaction. The dashed line indicates the zero-point vibrational energy of CH_3F .

respectively. Thus, as E_{coll} increases, the front-side attack cross sections approach the abstraction ones. Furthermore, at $E_{\text{coll}} = 80 \text{ kcal mol}^{-1}$, the retention cross sections are only an order of magnitude smaller than the inversion ones. Considering the shape of the excitation functions, i.e., nearly constant for inversion and a rapidly increasing concave-up for front-side attack retention, we can expect that at high E_{coll} ($>100 \text{ kcal mol}^{-1}$), the retention becomes the dominant mechanism for the $\text{F}^- + \text{CH}_3\text{F}$ $\text{S}_{\text{N}}2$ reaction. Seeing the significant front-side attack cross sections of the $\text{F}^- + \text{CH}_3\text{F}$ reaction at high E_{coll} , it is interesting to note that a direct dynamics study did not find front-side attack trajectories for the $\text{Cl}^- + \text{CH}_3\text{Cl}$ reaction at $E_{\text{coll}} = 100 \text{ kcal mol}^{-1}$.¹⁴ The double-inversion cross sections of the $\text{F}^- + \text{CH}_3\text{F}$ reaction are small (about an order of magnitude smaller than those of $\text{F}^- + \text{CH}_3\text{Cl}$). The double-inversion excitation function has a maximum around $E_{\text{coll}} = 60 \text{ kcal mol}^{-1}$ and then decreases with E_{coll} . We also investigated the induced-inversion pathway leading to an inverted reactant (inverted CH_3F without halogen exchange). The induced-inversion goes through the $\text{FH} \cdots \text{CH}_2\text{F}^-$ saddle point, but the first inversion is not followed by a substitution, thereby resulting in an inverted reactant. The shape and threshold of the excitation functions of the induced- and double-inversions are similar, but the induced inversion has about 2–3 times larger cross sections.

Scattering angle (θ) and initial attack angle (α) distributions at different E_{coll} 's in the 1–80 kcal mol^{-1} range for the substitution reaction are shown in Figure 5. Attack angle is defined at $t = 0$ as the angle between the CF bond vector and the center of mass velocity vector of the reactant CH_3F . At $E_{\text{coll}} = 1 \text{ kcal mol}^{-1}$, the θ distribution is backward-forward symmetric, almost uniform in the $(-0.8, 0.8) \cos \theta$ range, and peaks at 0° and 180° directions. This shape suggests that the direct rebound (backward scattering), direct stripping (forward scattering), as well as the indirect mechanisms (random scattering directions) are all significant at low E_{coll} . At $E_{\text{coll}} = 1 \text{ kcal mol}^{-1}$, the α distribution is almost isotropic indicating a strong orientation effect due to the long-range ion-dipole interactions. In other words, at very low E_{coll} , the reactivity does not depend on the initial orientation of the reactants, and the attractive long-range interactions can steer the slow F^- and CH_3F into a reactive orientation. As E_{coll} increases, the θ distributions become more and more backward scattered indicating the dominance of the direct rebound mechanism. At $E_{\text{coll}} = 10 \text{ kcal mol}^{-1}$, the α distribution is already back-side (90° – 180°) dominant and the preference of the initial back-side attack orientations is more and more significant as E_{coll} increases. At $E_{\text{coll}} = 80 \text{ kcal mol}^{-1}$, it is interesting to find a bimodal α distribution with back-side dominance and a small broad peak at the front-side attack orientation. This second small peak corresponds to the front-side attack retention mechanism, which has an about 5% contribution to the $\text{S}_{\text{N}}2$ reactivity at $E_{\text{coll}} = 80 \text{ kcal mol}^{-1}$ (see Fig. 4).

Product relative translational energy (E_{trans}) and CH_3F internal energy (E_{int}) distributions at different E_{coll} 's in the 1–80 kcal mol^{-1} range for the substitution reaction are shown in Figure 6. At low E_{coll} , e.g., 1 and 10 kcal mol^{-1} , the translational energy distributions peak at nearly 0, and as E_{coll} increases, a second peak emerges at large energies while the

peak at 0 tends to vanish. The shift from cold to hot translational energy distributions with increasing E_{coll} correlates with the change of the dominant reaction mechanism from indirect to direct. At collision energies around 20 kcal mol^{-1} , it is interesting to observe a bimodal E_{trans} distribution with peaks at small and large translational energies. This shows that two different reaction mechanisms, indirect and direct, respectively, are dominant at this E_{coll} . At $E_{\text{coll}} = 80 \text{ kcal mol}^{-1}$, only one peak is seen, which corresponds to the direct mechanism. Since the reaction enthalpy of the $\text{F}^- + \text{CH}_3\text{F}$ $\text{S}_{\text{N}}2$ reaction is zero, $E_{\text{coll}} = (E_{\text{int}} - E_{\text{ZPE}}) + E_{\text{trans}}$ holds. (Note that E_{int} is relative to the minimum of the CH_3F potential.) According to quantum mechanics, $E_{\text{int}} - E_{\text{ZPE}} \geq 0$; thus, E_{trans} and E_{int} should be in the $(0, E_{\text{coll}})$ and $(E_{\text{ZPE}}, E_{\text{coll}} + E_{\text{ZPE}})$ ranges, respectively. However, due to the classical nature of the QCT method, the above relations may not be satisfied. Indeed, at low E_{coll} , the E_{trans} distributions have significant populations above E_{coll} . This correlates with the ZPE violation of E_{int} , which is serious at low E_{coll} , e.g., 1 kcal mol^{-1} , as mentioned previously when the ZPE-constrained cross sections were discussed (Fig. 4). As E_{coll} increases, the ZPE issue becomes less important. For example, at $E_{\text{coll}} = 80 \text{ kcal mol}^{-1}$, the ZPE violation is negligible; thus, E_{trans} is in the $(0, 80) \text{ kcal mol}^{-1}$ range. Note that $E_{\text{int}} \leq E_{\text{coll}} + E_{\text{ZPE}}$ always holds, because E_{trans} cannot be less than 0. The shape of the E_{int} distributions depends on E_{coll} . At low E_{coll} , the E_{int} distributions peak close to the maximum available energy ($E_{\text{coll}} + E_{\text{ZPE}}$), and this peak shifts toward the lower energy end of the distributions as E_{coll} increases. This finding correlates with the shape of the E_{trans} distributions. Of course, this is expected, because the sum $E_{\text{int}} + E_{\text{trans}}$ is a constant at a given E_{coll} , resulting in E_{int} and E_{trans} distributions that are almost mirror images of each other (Fig. 6).

Due to the fact that identical reactant and product wells of the PES of the $\text{F}^- + \text{CH}_3\text{F}$ $\text{S}_{\text{N}}2$ reaction are separated by a central saddle point slightly below the reactant/product asymptotes, one can expect that barrier recrossing may play a significant role in the dynamics. We investigate the recrossing effects and present the cross sections as a function of the number of crossings in Figure 7. Odd number of crossings means

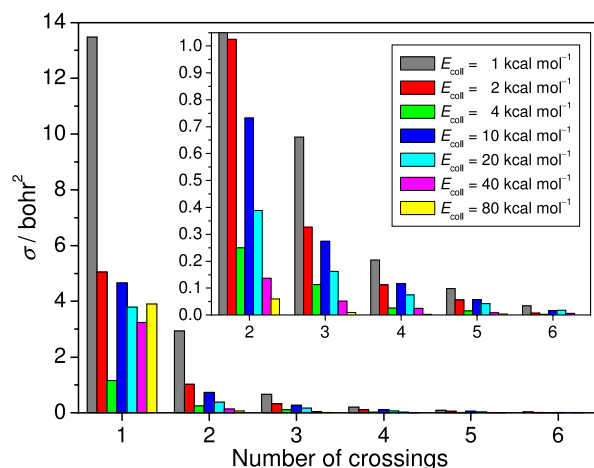


FIG. 7. Integral cross sections of the $\text{F}^- + \text{CH}_3\text{F}$ $\text{S}_{\text{N}}2$ reaction as a function of the number of saddle-point crossings at different collision energies. Odd and even number of crossings mean reactive and non-reactive trajectories, respectively.

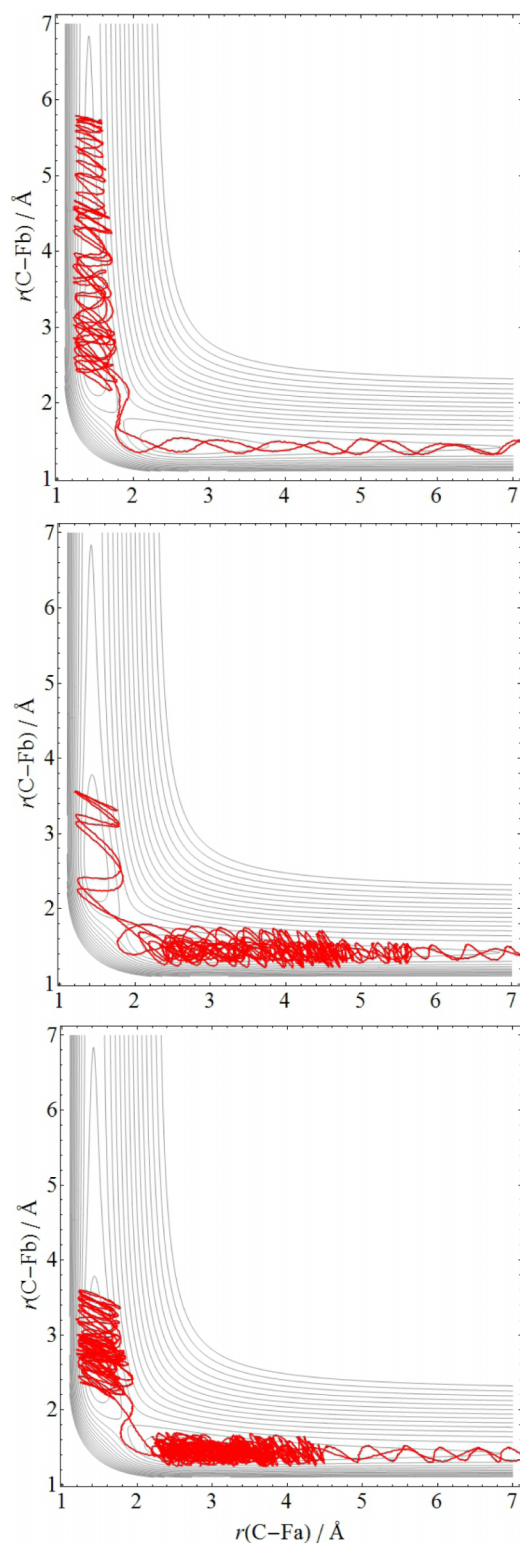


FIG. 8. Plots of three different types of $F^- + CH_3F_b \rightarrow CH_3F_b + F^-$ non-reactive recrossing trajectories at $E_{\text{coll}} = 10 \text{ kcal mol}^{-1}$ trapped in the exit channel for 2.2 ps (upper panel), in the entrance channel for 4.9 ps (middle panel), and in both the exit and entrance channels for 8.8 ps (lower panel).

reactive trajectories, whereas even number of crossings means non-reactive ones. Of course, most of the trajectories are non-reactive with zero crossing and most of the reactive trajectories cross the barrier only once, and the cross sections decrease rapidly with increasing number of crossings. However, at

low E_{coll} , a significant number of recrossing (2 crossings) non-reactive trajectories is found and we even see crossings 3 or more times. For example, at $E_{\text{coll}} = 1 \text{ kcal mol}^{-1}$, the cross sections are 13.5, 2.9, 0.7, 0.2, 0.1, and 0.0 bohr² for 1, 2, 3, 4, 5, and 6 crossings, respectively. Thus, the total reactive cross section is $13.5 + 0.7 + 0.1 = 14.3 \text{ bohr}^2$, whereas a cross section of $2.9 + 0.2 + 0.0 = 3.1 \text{ bohr}^2$ corresponds to those non-reactive trajectories that cross the barrier. As seen, if we considered all those trajectories that cross the barrier reactive, we would overestimate the cross sections by about 20%. At low E_{coll} , the recrossing probability remains similar, and even at $E_{\text{coll}} = 10 \text{ kcal mol}^{-1}$, the recrossing reduces the reactivity by 17%. As E_{coll} further increases the recrossing probability decreases as 12%, 5%, and 2% for $E_{\text{coll}} = 20, 40,$ and 80 kcal mol^{-1} , respectively. Typical recrossing trajectories are shown in Figure 8. As seen, we have found trajectories which go over the barrier fast and then trap in the product well and eventually recross the barrier and the reactants depart each other fast (upper panel). It is also possible that the trajectory spends only a short time in the product well before recrossing and then stays a longer time in the entrance well (middle panel). Finally, Figure 8 also shows a trajectory trapped in both the product and reactant wells (lower panel). We can conclude that the pre- and post-reaction complexes play a major role in the dynamics of the $F^- + CH_3F$ reaction.

V. SUMMARY AND CONCLUSIONS

Following our previous work on the $F^- + CH_3Cl$ reaction,^{11,12} we have developed a full-dimensional global analytical PES for the $F^- + CH_3F$ reaction, which accurately describes the Walden inversion S_N2 pathway, the front-side attack and double-inversion retention mechanisms as well as the proton-abstraction channel. The analytical PES is obtained by fitting about 50 000 *ab initio* energy points computed by an efficient explicitly correlated composite approach. The fitting basis is explicitly invariant under the permutation of the identical atoms (3 H and 2 F), which reduces the number of coefficients by a factor of about 9, resulting in 5850 coefficients for a 6th order fit. Note that for $F^- + CH_3Cl$, a 6th order fit would have resulted in about twice as many coefficients due to the lower permutational symmetry; thus, we used just a 5th order fit for $F^- + CH_3Cl$ which gave about 3300 coefficients.^{11,12}

We have determined the best technically feasible relative energies of the stationary points of the $F^- + CH_3F$ PES using the FPA approach. The present FPA study provides relativistic all-electron CCSDT(Q)/complete-basis-set quality relative energies which could serve as benchmark data for future studies of the $F^- + CH_3F$ system. The most important benchmark FPA classical(ZPE-corrected adiabatic) energies in kcal mol⁻¹, relative to $F^- + CH_3F$, can be summarized as follows:

- the central barrier height is $-0.45(-0.61)$,
- ion-dipole complex is at $-13.81(-13.56)$,
- H-bonded complex is at $-13.73(-13.52)$,
- front-side attack barrier height is $46.07(45.16)$,
- double-inversion barrier height is $29.18(26.07)$,
- proton-abstraction endothermicity is $42.54(38.11)$.

The analytical PES reproduces the benchmark FPA energies with excellent accuracy, since most of the FPA and PES values agree within $0.1 \text{ kcal mol}^{-1}$. This unusual agreement shows the accuracy of the 6th order fit and that of the composite *ab initio* energy points. We should note that the accuracy of the PES seems even better than one would expect. The fortuitously small deviations between the FPA and PES relative energies may be due to favorable error cancellations. On the basis of the FPA vs. PES comparisons at nine stationary points and the RMS fitting errors, we predict that the absolute average accuracy of the global PES up to $100 \text{ kcal mol}^{-1}$ is about $0.5 \text{ kcal mol}^{-1}$.

We have run about 2×10^6 trajectories on the new analytical PES. The cross sections of the substitution reaction are sensitive to the ZPE treatment and depend on E_{coll} at low collision energies, whereas above $E_{\text{coll}} = 10 \text{ kcal mol}^{-1}$, the excitation function is nearly constant without any significant ZPE effect. The proton-abstraction channel opens at around 40 kcal mol^{-1} and the abstraction cross sections increase rapidly with increasing E_{coll} . S_N2 retention trajectories have been found above $E_{\text{coll}} = 30 \text{ kcal mol}^{-1}$. In the E_{coll} range of about $30\text{--}50 \text{ kcal mol}^{-1}$, the retention trajectories go via the double-inversion mechanism, whereas at around $E_{\text{coll}} = 50 \text{ kcal mol}^{-1}$, the front-side attack pathway opens and quickly becomes the dominant retention mechanism. The front-side attack excitation function increases very rapidly with increasing E_{coll} . At $E_{\text{coll}} = 60, 70, \text{ and } 80 \text{ kcal mol}^{-1}$, $0.5\%, 2.4\%, \text{ and } 5.3\%$, respectively, of the reactive S_N2 events occur with the front-side attack retention mechanism. We may expect that the retention pathway could be the dominant S_N2 mechanism of the $F^- + \text{CH}_3\text{F}$ reaction at super high collision energies. The double-inversion mechanism was recently discovered for the $F^- + \text{CH}_3\text{Cl}$ reaction¹² and predicted to be a general mechanism for S_N2 reactions.¹³ The present dynamical study confirms the double-inversion pathway for another S_N2 reaction, though the double-inversion cross sections of the $F^- + \text{CH}_3\text{F}$ reaction are smaller than those of the $F^- + \text{CH}_3\text{Cl}$ system. Of course, this was expected, since the double-inversion barrier height of $F^- + \text{CH}_3\text{F}$ is about twice as high as that of $F^- + \text{CH}_3\text{Cl}$. We should emphasize that our analytical PES makes it possible to run hundreds of thousands of trajectories at each E_{coll} , which allows computing these small cross sections with reasonable accuracy.

The scattering angle distributions are backward-forward symmetric at low E_{coll} indicating direct rebound, direct stripping, and indirect mechanisms. As E_{coll} increases, the angular distributions shift toward backward scattering, showing that the direct rebound mechanism dominates at high E_{coll} . The initial attack angle distributions reveal that at low E_{coll} , the long-range attractive ion-dipole interactions steer the reactants into a reactive configuration regardless of the initial orientation. As E_{coll} increases, the back-side attack becomes the preferred initial orientation, and at very high E_{coll} , e.g., 80 kcal mol^{-1} , the front-side attack initial orientations show up in the attack angle distributions. The product relative translational energy and internal energy distributions are almost mirror images of each other due to the conservation of the total energy. The shape of the hotter and hotter translational energy distributions correlates with the dominance of the direct

rebound mechanism as E_{coll} increases. The simulations revealed significant amount of recrossing trajectories, especially at low E_{coll} . If one neglects the recrossing effects, the reaction cross sections can be seriously overestimated, e.g., by about 20% in the E_{coll} range of $1\text{--}10 \text{ kcal mol}^{-1}$.

The present study demonstrates again that the dynamics of a simple S_N2 reaction can be quite complex. The front-side attack retention mechanism can be increasingly important at higher collision energies. Furthermore, the double-inversion mechanism revealed for the $F^- + \text{CH}_3\text{Cl}$ reaction can occur for $F^- + \text{CH}_3\text{F}$ as well. The new analytical PES may inspire future quantum dynamical studies at least in reduced dimensions. Such quantum computations would be desired at low collision energies, where the present QCT results indicate serious zero-point energy effects. Furthermore, the present study may motivate experimental investigations of the proton-abstraction channel of the $F^- + \text{CH}_3\text{F}$ system and additional theoretical and/or experimental studies of other identity S_N2 reactions.

ACKNOWLEDGMENTS

G.C. was supported by the Scientific Research Fund of Hungary (OTKA, PD-111900) and the János Bolyai Research Scholarship of the Hungarian Academy of Sciences.

- ¹W. L. Hase, *Science* **266**, 998 (1994).
- ²J. L. Chabiny, S. L. Craig, C. K. Regan, and J. I. Brauman, *Science* **279**, 1882 (1998).
- ³L. Sun, K. Song, and W. L. Hase, *Science* **296**, 875 (2002).
- ⁴J. I. Brauman, *Science* **319**, 168 (2008).
- ⁵J. M. Gonzales, C. Pak, R. S. Cox, W. D. Allen, H. F. Schaefer III, A. G. Császár, and G. Tarczay, *Chem. - Eur. J.* **9**, 2173 (2003).
- ⁶J. Mikosch, S. Trippel, C. Eichhorn, R. Otto, U. Lourderaj, J. X. Zhang, W. L. Hase, M. Weidemüller, and R. Wester, *Science* **319**, 183 (2008).
- ⁷J. Zhang, Y. Xu, J. Chen, and D. Y. Wang, *Phys. Chem. Chem. Phys.* **16**, 7611 (2014).
- ⁸P. Manikandan, J. Zhang, and W. L. Hase, *J. Phys. Chem. A* **116**, 3061 (2012).
- ⁹R. Wester, *Phys. Chem. Chem. Phys.* **16**, 396 (2014).
- ¹⁰J. Xie, R. Otto, J. Mikosch, J. Zhang, R. Wester, and W. L. Hase, *Acc. Chem. Res.* **47**, 2960 (2014).
- ¹¹I. Szabó, A. G. Császár, and G. Czakó, *Chem. Sci.* **4**, 4362 (2013).
- ¹²I. Szabó and G. Czakó, *Nat. Commun.* **6**, 5972 (2015).
- ¹³I. Szabó and G. Czakó, *J. Phys. Chem. A* **119**, 3134 (2015).
- ¹⁴G. Li and W. L. Hase, *J. Am. Chem. Soc.* **121**, 7124 (1999).
- ¹⁵H. Tachikawa and M. Igarashi, *Chem. Phys. Lett.* **303**, 81 (1999).
- ¹⁶H. Tachikawa, M. Igarashi, and T. Ishibashi, *J. Phys. Chem. A* **106**, 10977 (2002).
- ¹⁷J. M. Bowman, G. Czakó, and B. Fu, *Phys. Chem. Chem. Phys.* **13**, 8094 (2011).
- ¹⁸G. Czakó and J. M. Bowman, *J. Phys. Chem. A* **118**, 2839 (2014).
- ¹⁹W. D. Allen, A. L. L. East, and A. G. Császár, in *Structures and Conformations of Non-Rigid Molecules*, edited by J. Laane, M. Dakkouri, B. van der Veken, and H. Oberhammer (Kluwer, Dordrecht, 1993), p. 343.
- ²⁰A. G. Császár, W. D. Allen, and H. F. Schaefer, *J. Chem. Phys.* **108**, 9751 (1998).
- ²¹T. B. Adler, G. Knizia, and H.-J. Werner, *J. Chem. Phys.* **127**, 221106 (2007).
- ²²K. A. Peterson, T. B. Adler, and H.-J. Werner, *J. Chem. Phys.* **128**, 084102 (2008); J. G. Hill, S. Mazumder, and K. A. Peterson, *ibid.* **132**, 054108 (2010).
- ²³W. J. Hehre, L. Radom, P. v. R. Schleyer, and J. A. Pople, *Molecular Orbital Theory* (Wiley, New York, 1986).
- ²⁴C. Møller and M. S. Plesset, *Phys. Rev.* **46**, 618 (1934).
- ²⁵R. J. Bartlett, C. E. Dykstra, and J. Paldus, in *Advanced Theories and Computational Approaches to the Electronic Structure of Molecules*, edited by C. E. Dykstra (Reidel, Dordrecht, 1984), p. 127.
- ²⁶K. Raghavachari, G. W. Trucks, J. A. Pople, and M. Head-Gordon, *Chem. Phys. Lett.* **157**, 479 (1989).

- ²⁷D. E. Woon and T. H. Dunning, Jr., *J. Chem. Phys.* **103**, 4572 (1995).
- ²⁸Y. Bomble, M. Kállay, J. Gauss, and J. F. Stanton, *J. Chem. Phys.* **123**, 054101 (2005).
- ²⁹M. Douglas and N. M. Kroll, *Ann. Phys.* **82**, 89 (1974).
- ³⁰H.-J. Werner, P. J. Knowles, G. Knizia, F. R. Manby, M. Schütz *et al.*, MOLPRO, version 2012.1, a package of *ab initio* programs, 2012, see <http://www.molpro.net>.
- ³¹Mrc, a quantum chemical program suite written by M. Kállay, Z. Rolik, I. Ladjánszki, L. Szegedy, B. Ladóczki, J. Csontos, and B. Kornis, see also, Z. Rolik and M. Kállay, *J. Chem. Phys.* **135**, 104111 (2011), www.mrcc.hu.
- ³²A. Karton and J. M. L. Martin, *Theor. Chem. Acc.* **115**, 330 (2006); W. Klopper and W. Kutzelnigg, *J. Mol. Struct.: THEOCHEM* **135**, 339 (1986); G. Tasi and A. G. Császár, *Chem. Phys. Lett.* **438**, 139 (2007).
- ³³T. Helgaker, W. Klopper, H. Koch, and J. Noga, *J. Chem. Phys.* **106**, 9639 (1997).
- ³⁴J. Zhang and W. L. Hase, *J. Phys. Chem. A* **114**, 9635 (2010).
- ³⁵J. Xie, J. Zhang, and W. L. Hase, *Int. J. Mass Spectrom.* **378**, 14 (2015).
- ³⁶T. J. Lee and P. R. Taylor, *Int. J. Quantum Chem.* **36**(S23), 199 (1989).
- ³⁷G. Czakó, I. Szabó, and H. Telekes, *J. Phys. Chem. A* **118**, 646 (2014).
- ³⁸B. J. Braams and J. M. Bowman, *Int. Rev. Phys. Chem.* **28**, 577 (2009).